Estimation of surface free energy at microstructured surface to investigate intermediate wetting state for partial wetting model

Yankun YU, ‡ [a] Dejian ZHANG ‡ [b] and Gyoko NAGAYAMA*[c]

While partial wetting at nano-/microstructured surfaces can be described using the intermediate wetting state between the Cassie–Baxter and Wenzel states, the limitations of the partial wetting model remain unclear. In this study, we performed surface free energy analysis at a microstructured Si-water interface from both theoretical and experimental viewpoints. We experimentally measured the water contact angle on microstructured Si surfaces with square holes and compared the measured values with theoretical predictions. Furthermore, the surface free energy was analyzed using the effective wetting area estimated from the measured contact angle and electrochemical impedance spectroscopy results. We verified the validity of the partial wetting model for fabricated Si surfaces with a hole aperture a less than 230 μm and a hole height h of 12 μm, and for $a < 400$ μm, $h = 40$ μm. The model was found to be applicable to microstructured Si surfaces with $a/h < 10$.

1. Introduction

Micro-/nanostructured surfaces are encountered in a wide range of applications; for instance, in micro-/nanofluidic systems,[1,2] on functional surfaces,[3–9] on tribological surfaces,[10–12] and at thermal transport interfaces.[13–18] In particular, the wettability of structured surfaces has attracted considerable interest over the past few years, and many theoretical and experimental studies have been conducted on it.

Generally, the surface wettability can be characterized by the apparent macroscopic contact angle, which depends on the properties of the liquid and solid. For a flat solid surface, the contact angle of a droplet depends only on the surface chemical composition, while, for a structured surface, the contact angle depends on both the chemical composition of material and geometric morphology of the surface. The wettability of structured surfaces is related to the wetting state, which is determined by the ratio of the wetting area to the total solid surface area beneath a droplet. Notably, the wetting state for the structured surface of a given material is determined by the real solid–liquid contact area beneath a droplet.

Over the past several decades, several models have been proposed to elucidate wetting states at solid–liquid interfaces with surface structures. The Cassie–Baxter state[19] is a non-wetting state that corresponds to the minimum solid–liquid contact area beneath a droplet, while the Wenzel state[20] is a fully wetting state characterized by the maximum solid–liquid contact area. Wetting states different from these two states have also been widely observed during wetting transitions[21–27] and gradient wetting.[28–30] Min et al. proposed a hybrid wetting model involving a locally suspended and pillar/hole arrays for a nanostructured surface.[29] Another study proposed a partial wetting model for an intermediate wetting state between the Cassie–Baxter and Wenzel states in the case of static wetting.[31] In the model, an effective wetting ratio f, defined as the proportion of liquid wetting into the structures, was used to determine the intermediate wetting state. For a given surface structure, f is 1 for the fully wetting Wenzel state, 0 for the nonwetting Cassie–Baxter state, and between 0 and 1 for an intermediate wetting state.

Although it is easy to directly measure the apparent contact angle, this parameter does not provide information about the wetting state at the solid–liquid interface involved in partial wetting. Researchers have used an approach involving surface free energy (or Gibbs energy) minimization to obtain information about the wetting state and contact angle. Rohrs et al. presented a model based on a sophisticated Gibbs energy model to describe "partial penetration in the Cassie–Baxter state".[32] Kaufman et al. developed a wetting model that could be used along with a "local force (and energy) equation" to predict the contact angle at a textured surface.[33] Chen et al. studied the critical conditions required for the existence of a hemi-wicking state in the vicinity of a contact line outside a droplet on patterned surfaces.[34] Furthermore, Kita et al. performed surface energy analysis for drop motion and found that drop mobility induced via wettability contrasts was initiated by excess surface free energy because of drop deformation.[35] However, these studies did not focus sufficiently on the surface free energy related to the solid–liquid interfacial area in a wetting state intermediate between the Wenzel and Cassie–Baxter states, which is known to lie between the surface free energies for these two states. Further investigations of the surface free energy for all these wetting states are required to clarify the intermediate wetting state for the partial wetting model.

Intermediate-like wetting states have been qualitatively investigated through theoretical analyses[36,37] and experimental observations.[38–42] However, few studies have quantitatively evaluated intermediate wetting states, owing to difficulties in

performing precise measurement. To overcome the challenges faced in performing a quantitative investigation, we have previously employed electrochemical impedance spectroscopy (EIS) to estimate the effective wetting area for the intermediate wetting state.[43,44] This technique can also be used to determine the surface free energy for the intermediate wetting state.

While extensive studies have been conducted on the superhydrophobicity of micropillar-structured surfaces, less attention has been paid to microhole-structured surfaces, especially the wetting state in a hole. In this study, we fabricated microstructured Si surfaces with square holes through Bosch deep reactive ion etching to investigate the wetting state in a hole. We performed surface free energy analysis at a microstructured Si-water interface from both theoretical and experimental viewpoints. Moreover, experimentally measured water contact angle and the effective wetting area on the Si surfaces were compared with theoretical predictions of the Wenzel, Cassie–Baxter, and partial wetting models. We estimated the surface free energy of a microstructured Si-water interface from the measured contact angle and effective wetting area. Here, apart from describing our study and presenting its results, we discuss the suitability of the partial wetting model for the fabricated Si surfaces.

2. Methods

2.1 Theoretical models

The surface free energy of a static droplet on a flat and smooth solid surface in an equilibrium system was determined using a thermodynamic approach. We ignored gravity, the Laplace pressure of the droplet, the line tension, and the contact angle hysteresis. As illustrated in Fig. 1(a), the intrinsic contact angle θ_Y formed at the liquid−solid−vapor triple line of the droplet was considered. The parameter θ_Y can be expressed using Young's equation[45]:

$$\cos \theta_Y = \frac{\gamma_{sv} - \gamma_{sl}}{\gamma_{lv}} \tag{1}$$

where γ_{sl}, γ_{sv}, and γ_{lv} are the solid–liquid, solid–vapor, and liquid–vapor interfacial surface tensions, respectively. The total surface free energy E of the system shown in Fig. 1(a) can be calculated as follows:
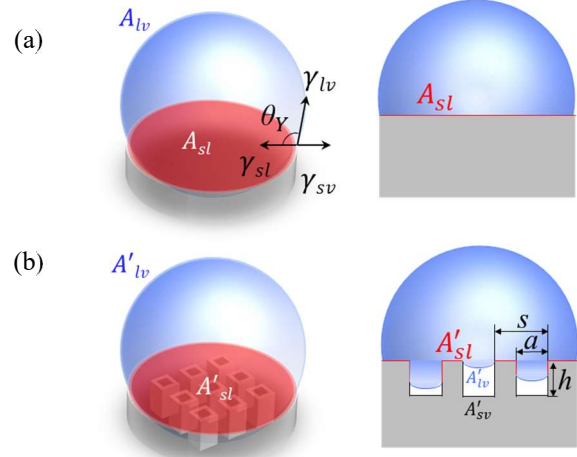
Fig. 1 Schematic of interfacial contact areas for a liquid droplet on (a) a flat surface and (b) a structured surface.

$$E = A_{sl}\gamma_{sl} + A_{sv}\gamma_{sv} + A_{lv}\gamma_{lv} \tag{2}$$

where A_{sl}, A_{sv}, and A_{lv} are the interfacial contact areas corresponding to the interfacial surface tensions (see Ref. [44] for details). Here, A_{sl} is referred to the solid–liquid interfacial contact area beneath the droplet, and A_{sv} can be ignored under the assumption that the contact line width is much smaller than the droplet size.

For a structured surface, the wettability inside the structures can be assumed to be identical to that of a flat surface. The total surface free energy E' at the structured surface of the system shown in Fig. 1(b) can be expressed as

$$E' = A'_{sl}\gamma_{sl} + A'_{sv}\gamma_{sv} + A'_{lv}\gamma_{lv} \tag{3}$$

Table 1   Interfacial surface areas between a droplet and the underlying surface for three wetting states.

	A'_{sl}	A'_{sv}	A'_{lv}
Cassie–Baxter state	ΦA_{sl}	$(r_w - \Phi)A_{sl}$	$A_{lv} + (1 - \Phi)A_{sl}$
Wenzel state	$r_w A_{sl}$	0	A_{lv}
Intermediate wetting state	$[\Phi + (r_w - \Phi)f]A_{sl}$	$(r_w - \Phi)(1 - f)A_{sl}$	$A_{lv} + (1 - \Phi)(1 - f)A_{sl}$

where A'_{sl}, A'_{sv}, and A'_{lv} are the solid–liquid, solid–vapor, and liquid–vapor contact areas at the structured surface. These interfacial contact areas depend on the wetting state beneath the droplet, and they can be calculated from A_{sl} and A_{lv}. Table 1 lists the expressions for the interfacial contact areas; r_w is the surface area increment ratio, Φ is the solid fraction, and f is the effective wetting ratio. These parameters along with A_{sl} can be calculated at the surface of any given geometrical structure.

Since the interfacial tension between a liquid and a solid is difficult to measure in practice, γ_{sl} is calculated using the Owens–Wendt–Rabel–Kaelble (OWRK) model:[46–49]

$$\gamma_{sl} = \gamma_{sv} + \gamma_{lv} - 2\left(\sqrt{\gamma_s^d \cdot \gamma_l^d} + \sqrt{\gamma_s^p \cdot \gamma_l^p}\right) \qquad (4)$$

where the interfacial interactions γ_s^d and γ_l^d are the disperse components and γ_s^p and γ_l^p are the polar components. Table 2 lists the surface tensions of water and Si.[50] The solid–vapor interfacial tension results in a surface tension of 47.36 mN/m, and the liquid–vapor interfacial tension results in a surface tension of 72.80 mN/m. Thus, on the basis of the OWRK model, the solid–liquid interfacial tension results in a surface tension of 42.56 mN/m.

Table 2   Surface tensions of water and Si.

	γ^d (mN/m)	γ^p (mN/m)	γ (mN/m)
Water	21.80	51.00	72.80
Si	46.40	0.96	47.36

2.2 Microstructured Si surface fabrication

A p-type Si(100) wafer was used to fabricate microstructured surfaces. It was cleaned using acetone, isopropanol, and pure water sequentially in an ultrasonic bath for 10 min. Subsequently, a photoresist was deposited on its surface, and the wafer was patterned using maskless lithography with a micropatterned area of 8 mm × 8 mm. A deep reactive ion etching system (Samco, RIE-400iPB) was used to form microstructures with square holes on the Si wafer. The photoresist was then removed through O_2 plasma treatment for 30 s, and the Si wafer was cleaned with
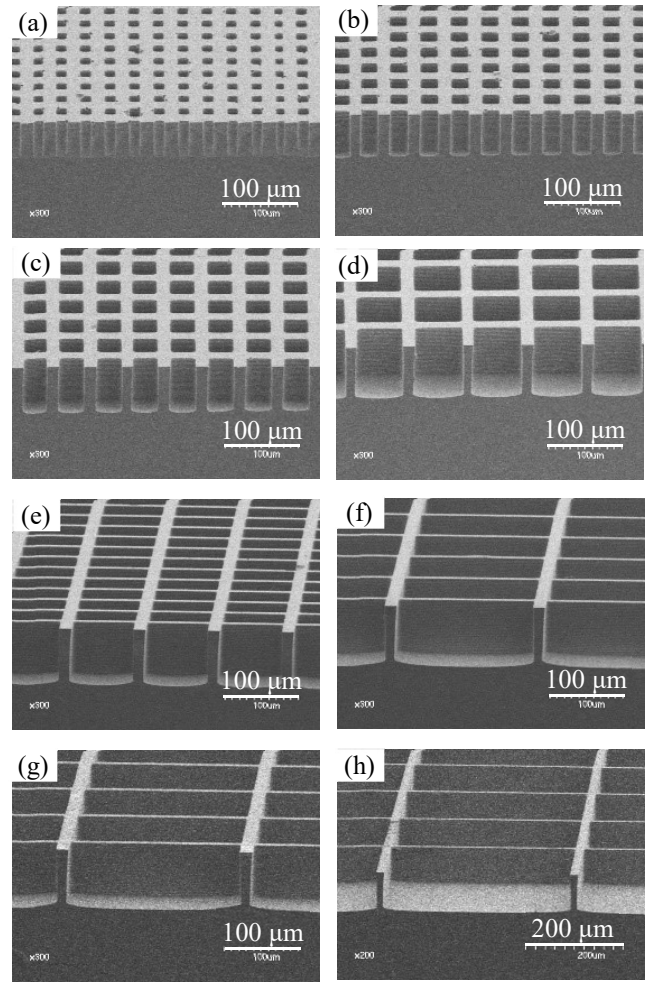

Fig. 2 Typical scanning electron microscope images of fabricated microstructured Si surfaces. The square holes had a height of 12 μm and apertures of (a) 12, (b) 20, (c) 30, (d) 60, (e) 80, (f) 180, (g) 230, and (h) 380 μm.

acetone and deionized water in an ultrasonic bath for 10 min. The cleaned wafer was cut into squares with dimensions of 15 mm × 15 mm. Fig. 2 shows typical scanning electron microscope images of fabricated Si surfaces with square holes.

Table 3   Parameters of microstructured Si surfaces.

a [μm]	s [μm]	Φ [-]	f [-]	r_w [-]	
				$h = 12$ μm	$h = 40$ μm
12	32	0.86	0.04	1.56	2.88
20	40	0.75	0.08	1.60	3.00
30	50	0.64	0.13	1.58	2.92
60	80	0.44	0.22	1.45	2.50
80	100	0.36	0.26	1.38	2.28
180	200	0.19	0.39	1.22	1.72
230	250	0.15	0.43	1.18	1.59
380	400	0.10	0.50	1.11	1.38

The geometrical parameters of the 16 surfaces fabricated in this study are presented in Table 3. The square holes had an aperture a in the range of 12–380 μm, a height h of 12 μm or 40 μm, and a pitch s in the range of 32–400 μm. The surface area increment ratio, solid fraction, and effective wetting ratio were calculated using the expressions $r_w = 1 + 4ah/s^2$, $\Phi = 1 - (a/s)^2$, and $f = 1 - \Phi^{D-2}$ (where fractal dimension $D = 2.3$), respectively.[31]

2.3 Contact angle measurement

Before contact angle measurement, the Si samples were carefully cleaned as follows. They were immersed in ultrasonic baths of (1) acetone (for 10 min), (2) isopropyl alcohol (for 10 min), and (3) deionized water (for 10 min) to extract surface impurities. Then, they were immersed in a 1% buffered hydrofluoric acid solution for 10 min to remove the natural oxide layer on their surfaces. Finally, the samples were rinsed in purified water for 5 min in an ultrasonic bath.

The water contact angle was measured in a cell with a constant temperature of 20 °C and a relative humidity (RH) of 40% (details are provided in the supplemental materials of Ref. 31). A 4 μl deionized water droplet was carefully placed on the Si surfaces using a micropipette. The contact angle was measured within one minute of the droplet being placed on a Si surface, and a side-view image was recorded using a digital microscope (Keyence, VHX-200). More than five measurements were performed on each sample surface to obtain the static water contact angle. The standard deviation of the contact angle measurements was about 5.36°, and the contact angle on a flat Si surface, θ_Y, was 76.72° ± 2.62°.

2.4 EIS measurement

The cleaning procedure described in Section 2.3 was repeated before EIS measurements. EIS was performed using an electrochemical workstation (BioLogic, SP-200) and a three-electrode testing system in a room with a constant temperature of 20 °C and an RH of 40%. The three-electrode testing system comprised a glass testing container, Si samples as the working electrode, a platinum wire as the counter electrode, and a silver–silver chloride electrode as the reference electrode. The working electrode had an area of 8 mm × 8 mm that was exposed to the electrolyte, which was purified water in this study. The testing system was covered by an electromagnetic shielding mesh during measurements.

The EIS measurement system was initially stabilized when the vibration of the open circuit potential was lower than 0.05 V for 1 min. The frequency range employed was 1 MHz to 100 mHz, and the excitation signal amplitude was 10 mV. The EIS measurement was repeated five times for each sample, and EIS spectra of 80 measurements were collected for further analysis on the ZSimpWin software.

3. Results and discussion

3.1 Contact angle
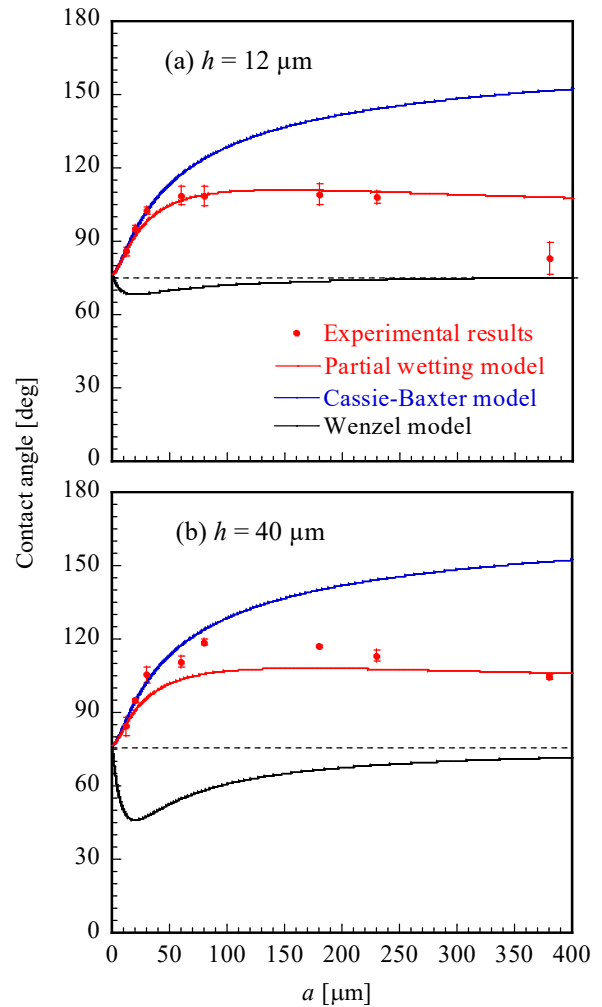
Fig. 3 Plots of the contact angle versus the hole aperture a of micropatterns for hole heights h of (a) 12 and (b) 40 μm. The dotted line represents the experimentally obtained contact angle on the flat Si surface.

Fig. 3 shows plots of the contact angle versus the square hole aperture a of micropatterns. The parameter θ_Y is shown by a dotted line, and contact angles measured on microstructured surfaces are shown by red solid circles. Clearly, all of the contact angles measured on the microstructured surface were greater than θ_Y. The measured contact angle increased with a for $a < 100$ μm, and it leveled off in the region 100 μm $< a <$ 230 μm. In the case of $h =$ 12 μm, the measured value was close to θ_Y for $a = 380$ μm. The contact angle predicted by the Cassie–Baxter model (blue solid line) monotonically increased as a increased, and that predicted by the partial wetting model (red solid line) increased with a for $a < 100$ μm but leveled off for $a > 100$ μm. The values predicted by the Wenzel model (black solid line) formed a V-shaped curve, with the minimum value occurring at $a = 20$ μm. As expected, the values predicted by the partial wetting model were between those predicted by the Cassie–Baxter and Wenzel models.

As shown in Fig. 3, there was a significant discrepancy between the experimental contact angle and the Wenzel model's prediction. The experimental results also deviated from the Cassie–Baxter model for $a > 30$ µm, with the deviation at $h = 12$ µm being greater than that at $h = 40$ µm. On the other hand, the experimental contact angles generally agreed with the values predicted by the partial wetting model for both h values, even when experimental errors were considered.

3.2 Effective wetting area

The EIS data were analyzed using equivalent electrical circuits to estimate the ratio of the solid–liquid contact area on a microstructured surface to that on the flat surface.[43,44] The effective wetting area at the structured solid–liquid interface was equivalent to A'_{sl}, and hence we have

Fig. 4 Plots of the solid–liquid interface area ratio A'_{sl}/A_{sl} versus the hole aperture of the micropatterns for (a) $h = 12$ µm and (b) $h = 40$ µm.

$$\frac{A'_{sl}}{A_{sl}} = \frac{|Z|}{|Z'|} \tag{5}$$

where Z and Z' are the electrochemical impedances for the flat and microstructured surfaces, respectively.

Fig. 4 shows plots of the area ratio A'_{sl}/A_{sl} versus a. The solid red circles represent experimental EIS results, and the continuous curves represent theoretical predictions obtained with the expressions in Table 1. Apparently, the experimental values of A'_{sl} were smaller than A_{sl}, and they decreased with an increase in a (except for the cases with $a \geq 230$ µm and $h = 12$ µm). The experimental values generally showed good agreement with the predictions of the partial wetting model but deviated from the predictions of the Wenzel and Cassie–Baxter models. As mentioned in Section 3.1, the experimental contact angles partially agreed with the predictions of the Cassie–Baxter model. However, the effective wetting area determined from EIS measurements deviated from that predicted by the Cassie–Baxter model. This suggests that the effective wetting area may be more suitable than the contact angle for describing the wetting state.

During the EIS measurement, a hydrostatic pressure was acting at the solid–liquid interface (see Supplementary Information of Ref. 44). Therefore, the experimental values of A'_{sl}/A_{sl} for $h = 40$ µm were slightly greater than the predictions of the partial wetting model. Notably, the hydrostatic pressure had little effect on the experimental results for $h = 12$ µm.

3.3 Surface free energy based on partial wetting model

To estimate the surface free energy E' (Eq. (2)), we should know the experimental value of f. Two methods were adopted to calculate f; one employed measured contact angles and the other involved the value of A'_{sl}/A_{sl}.

3.3.1 Surface free energy E'_θ. In the partial wetting model, the contact angle at a structured surface, θ, is expressed as

$$\cos\theta = (\Phi + (r_w - \Phi)f)\cos\theta_Y \\ +(1-\Phi)(1-f)\cos180° \quad . \tag{6}$$

Therefore, f becomes

$$f = \frac{(\cos\theta + 1) - (\cos\theta_Y + 1)\Phi}{(r_w - \Phi)\cos\theta_Y + (1-\Phi)} \quad . \tag{7}$$

Since the geometrical parameters Φ and r_w are constant for a given structure, the surface free energy E'_θ can be obtained by substituting the experimentally obtained f in Eq. (7) into Eq. (2).

Fig. 5 shows the values of E'_θ at microstructured Si surfaces with $h = 12$ µm and $h = 40$ µm. The dashed black line represents the surface free energy E on the flat Si surface. Clearly, E'_θ was greater than E for both heights, and E'_θ increased with a and reached the maximum value at
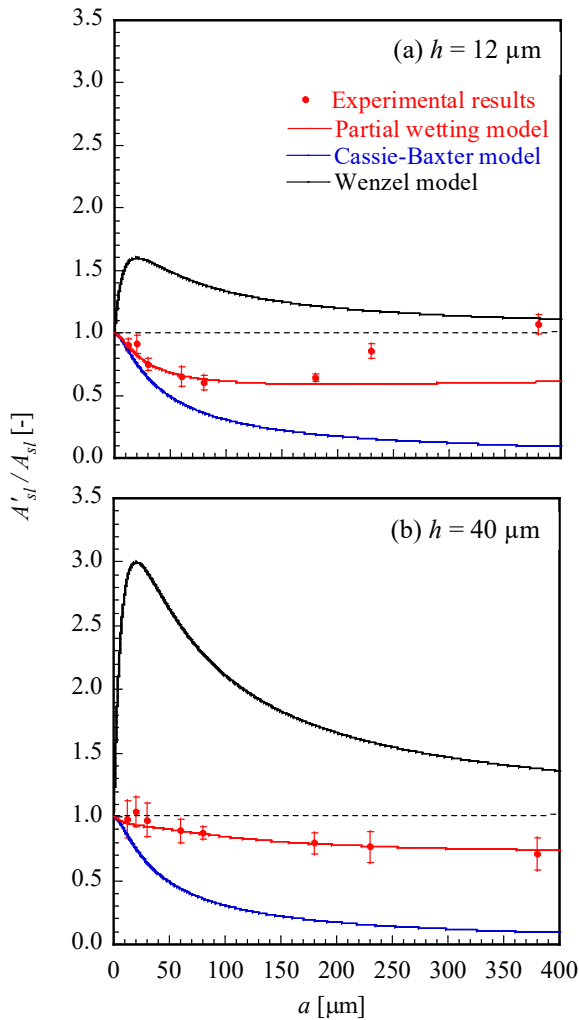
approximately $a = 30$ μm. However, for $a > 30$ μm, it gradually decreased with an increase in a.

Although E'_θ generally agreed with the predictions of the partial wetting model for $h = 12$ μm and $h = 40$ μm, it coincided with the predicted value for the flat surface at $a = 380$ μm for $h = 12$ μm. E'_θ for $h = 40$ μm was slightly greater than the prediction of the partial wetting model. However, E'_θ deviated from the prediction of the Wenzel model in the entire range of a and from the prediction of the Cassie–Baxter model for $a > 80$ μm.

3.3.2　Surface free energy E'_A. In Table 1, the area A'_{sl} of the partial wetting model is given by

$$A'_{sl} = (\Phi + (r_w - \Phi)f)A_{sl} \quad , \tag{8}$$

therefore, f becomes

$$f = \frac{\dfrac{A'_{sl}}{A_{sl}} - \Phi}{r_w - \Phi} \quad . \tag{9}$$

Since A'_{sl}/A_{sl} can be determined using the EIS method, the surface free energy E'_A can be obtained by substituting the experimental f of Eq. (9) into Eq. (2).

As shown in Fig. 5, E'_A and E'_θ showed similar dependence on a irrespective of the hole height. In the case of $h = 12$ μm, E'_A was comparable to E'_θ, except at $a = 230$ μm, and it was consistent with the partial wetting model for $a \leq 180$ μm. In the case of $h = 40$ μm, E'_A was smaller than E'_θ and showed better agreement with the partial wetting model than E'_θ. The difference between E'_A and E'_θ might have resulted from the measurement error of the effective wetting area, resulting from the presence of the hydrostatic pressure mentioned in Section 3.2.

3.3.3　Theoretical surface free energy. The theoretical surface free energies of the partial wetting model, Cassie–Baxter model, and Wenzel model are shown in Fig. 5. The values of the partial wetting and Wenzel models form a downward-facing curve, with the maximum value lying in the range of 20 μm $< a <$ 80 μm. However, the theoretical surface free energy of the Cassie–Baxter model monotonically increases for $h = 12$ μm, while a downward-facing curve appears for $h = 40$ μm. The three models are almost identical for $a < 20$ μm, while they are in descending order of magnitude for $a > 20$ μm. Table 4 lists the extreme values of the theoretical free energy calculated using the MATLAB software, and they support the experimental observations. Apparently, the partial wetting model described the experimental surface free energy well in the investigated cases. However, it appears to be applicable only to cases of small a or large h (i.e., small a/h). The cases where this model is applicable are discussed in Section 3.4.

Table 4　Extreme values ($\partial E'/\partial a = 0$) of theoretical surface free energy for the three wetting states.

Wetting states ╲ a [μm]	$h = 12$ μm	$h = 40$ μm
Cassie–Baxter state	NA	33.85
Intermediate wetting state	49.41	26.98
Wenzel state	20.00	20.00
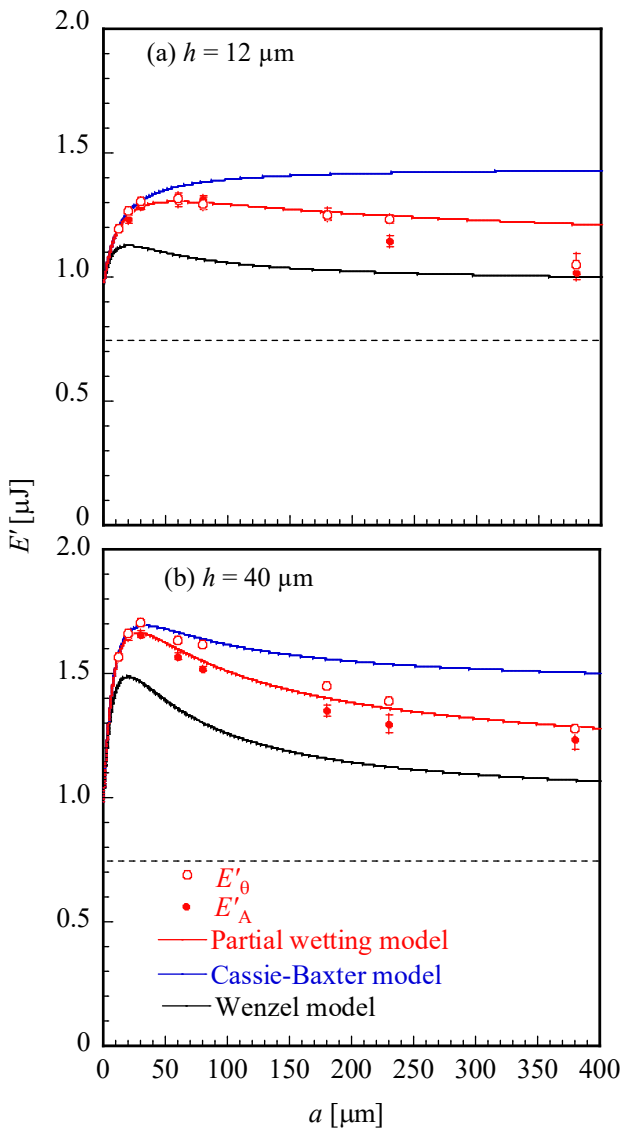
Fig. 5 Plots of the surface free energy versus the hole aperture of micropatterns for (a) $h = 12$ μm and (b) $h = 40$ μm. The dotted line represents the experimental surface free energy on the flat Si surface.
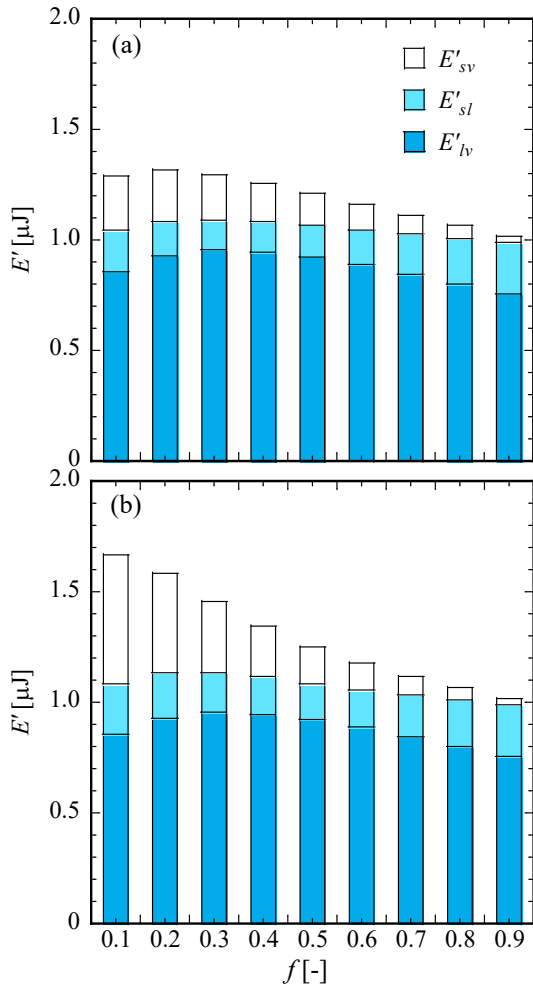
Fig. 6 Theoretical surface free energy of the partial wetting model versus the effective wetting ratio f for (a) $h = 12$ μm and (b) $h = 40$ μm.

3.3.4 Contributions of interfacial surface free energy to intermediate wetting state. Fig. 6 shows the contributions of the interfacial surface free energies E'_{sv}, E'_{sl}, and E'_{lv} to the intermediate wetting state for the partial wetting model. For both cases $h = 12$ μm and $h = 40$ μm, the liquid–vapor interfacial free energy E'_{lv} contributed significantly to the total surface free energy in the full range of f. Although a slight variation in the solid–liquid interfacial free energy E'_{sl} is apparent in Fig. 6, the sum of E'_{sl} and E'_{lv} contributed uniformly to the total surface free energy. However, the solid–vapor interfacial free energy E'_{sv} decreased as f increased, implying that E'_{sv} was dominant in the intermediate wetting state. In other words, a reduction in E'_{sv} resulted in a wetting transition from the Cassie–Baxter state to the Wenzel state.

In the present study, each experimental datum corresponded to a stable/metastable wetting state, without any spontaneous dynamic wetting transition. For a given surface structure, a wetting transition from the Cassie–Baxter state to either an intermediate state or the Wenzel state might occur with the aid of an external force. Such a process is likely to accompany a reduction in E'_{sv}.
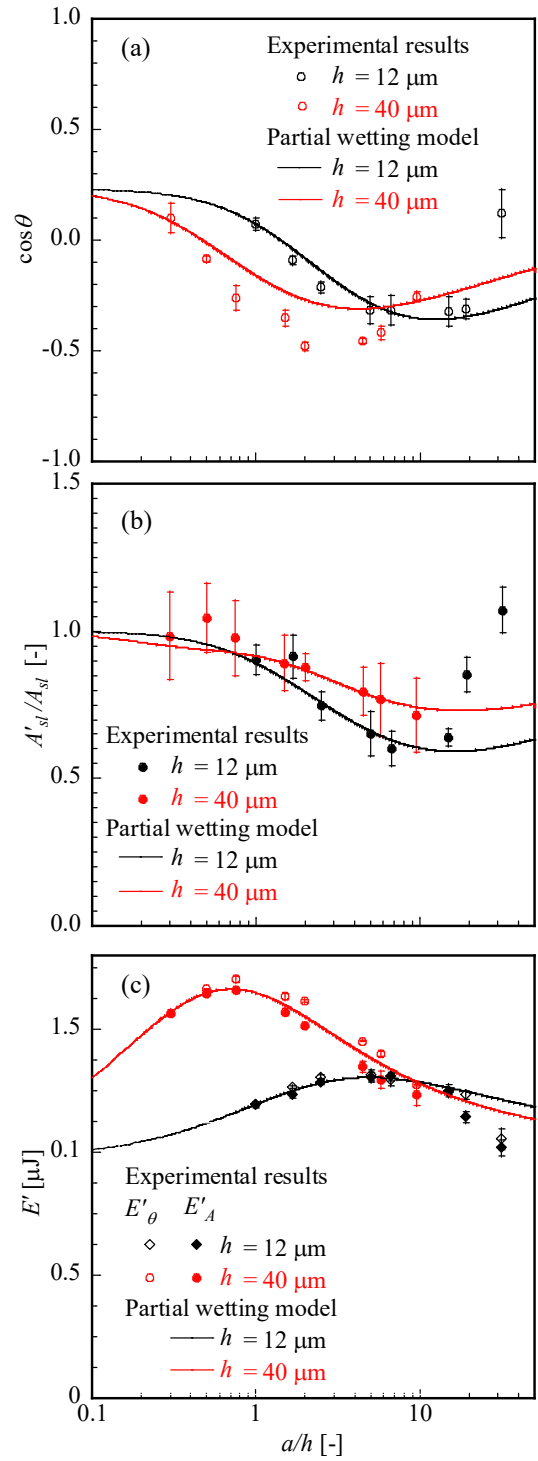
Fig. 7 Effect of ratio a/h on (a) contact angle, (b) solid–liquid interface area ratio A'_{sl}/A_{sl}, and (c) surface free energy.

3.4 Validation of partial wetting model

According to the Young–Laplace equation, a smaller a results in a larger capillary force. Therefore, a hole with a smaller a can be expected to lead to a larger effective wetting area. In particular, a small hole height h might limit capillary penetration through the hole. Fig. 7 shows plots of the contact angle, A'_{sl}/A_{sl}, and surface free energy against

a/h. Evidently, while the experimental values agree well with the predictions of the partial wetting model for $a/h < 10$, they deviate from the theoretical predictions for $a/h > 10$, where the structured surface morphologically resembles the flat surface.

In this study, we used monocrystalline Si as the model material for our investigation. Since the measured contact angle of the flat Si surface was close to 90°, the wettability of a structured Si surface might be hydrophobic or hydrophilic because of the surface geometric morphology. In particular, the geometrical parameters such as a, a/h, r_w, and Φ were dominant at the microhole-structured Si surfaces for an intermediate wetting state. The validity of the partial wetting model was successfully verified for the investigated surfaces with $a/h < 10$.

Discrepancies between experimental results for micropillar-structured surfaces and predictions of the partial wetting model have been previously reported.[51–53] They can be explained by the following reasons: (1) The surface roughness or undulation caused during the fabrication process (e.g., coating) was ignored, and the coating on the micropillars was not guaranteed to be uniform and to have the same thickness as that on a flat surface. (2) The contact angles at the flat surface with coating used in the studies were much lower or higher than 90°, and (3) the spacing between pillars at the micropillar-structured surfaces was open to the atmosphere. Since micropillars are usually fabricated with a hydrophobic coating, the synergetic effects of the surface structure and coating could induce superhydrophobicity at micropillar-structured surfaces. The verification of the partial wetting model requires accurate measurements of the contact angle on a pure structured surface without contamination, coating, etc.

Future work should investigate the disagreement between experimental results at micropillar-structured surfaces and the predictions of the partial wetting model.

4. Conclusions

In this work, surface free energy analysis at a microstructured Si-water interface was performed from both theoretical and experimental viewpoints. We estimated the effective wetting ratio from the measured contact angle and EIS results, and the surface free energy was analyzed using the experimentally obtained effective wetting ratio. The theoretical surface free energy predicted by the partial wetting model roughly agreed with the experimental value for a microstructured Si-water interface. The hole aperture range in which the partial wetting model was effective was below 230 μm for a hole height of 12 μm and below 400 μm for a hole height of 40 μm. The presented results imply that the partial wetting model is applicable to microhole-structured Si surfaces that satisfy the condition $a/h < 10$.

Author contributions

Yankun Yu: Investigation, Methodology, Data curation, Formal analysis, Writing - original draft. Dejian Zhang: Investigation, Methodology, Formal analysis, Validation, Writing – review & editing, Funding acquisition. Gyoko Nagayama: Conceptualization, Methodology, Data curation, Formal analysis, Supervision, Writing - review & editing, Funding acquisition.

Conflicts of interest

The authors declare no competing financial interest.

Acknowledgements

References

1 G. Nagayama, T. Tsuruta and P. Cheng, *Int. J. Heat Mass Transfer*, 2006, **49**, 4437–4443.
2 Y. Xu, *Adv. Mater.*, 2018, **30**, 1702419.
3 F. Chu, Z. Ni, D. Wen, Y. Feng, S. Li, L. Jiang and Z. Dong, *Adv. Funct. Mater.*, 2022, **32**, 2203222.
4 Y. Jiang and C.-H. Choi, *Adv. Mater. Interfaces*, 2021, **8**, 2001205.
5 S. Adera, R. Raj, R. Enright and E. N. Wang, *Nat. Commun.*, 2013, **4**, 2518.
6 D. Ebert and B. Bhushan, *J. Colloid Interface Sci.*, 2012, **368**, 584–591.
7 W. Li and A. Amirfazli, *Soft Matter*, 2008, **4**, 462–466.
8 Y.-L. Zhang, H. Xia, E. Kim and H.-B. Sun, *Soft Matter*, 2012, **8**, 11217–11231.
9 T. Kong, G. Luo, Y. Zhao and Z. Liu, *Adv. Funct. Mater.*, 2019, **29**, 1808012.
10 M. Conradi, A. Drnovšek and P. Gregorčič, *Sci. Rep.*, 2018, **8**, 7457.
11 Y. Guo, X. Zhang, X. Wang, Q. Xu and T. Geng, *J. Mater. Sci.*, 2020, **55**, 11658–11668.
12 E. Brinksmeier, O.Riemer, and S.Twardy, *Int. J. Mach. Tools Manuf.*, 2010, **50**, 425–430.
13 D. Orejon, O. Shardt, N. S. K. Gunda, T. Ikuta, K. Takahashi, Y. Takata and S. K. Mitra, *Int. J. Heat Mass Transf.*, 2017, **114**, 187–197.
14 L. Wang, Z. Tian, G. Jiang, X. Luo, C. Chen, X. Hu, H. Zhang and M. Zhong, *Nat. Commun.*, 2022, **13**, 378.
15 Y. Xu, D. Kraemer, B. Song, Z. Jiang, J. Zhou, J. Loomis, J. Wang, M. Li, H. Ghasemi, X. Huang, X. Li and G. Chen, *Nat. Commun.*, 2019, **10**, 1771.
16 M. Jiang, Y. Wang, F. Liu, H. Du, Y. Li, H. Zhang, S. To, S. Wang, C. Pan, J. Yu, D. Quéré and Z. Wang, *Nature*, 2022, **601**, 568–572.

17 A. R. Betz, J. Xu, H. Qiu and D. Attinger, *Appl. Phys. Lett.*, 2010, **97**, 141909.

18 G. Nagayama, M. Kawagoe, A. Tokunaga and T. Tsuruta, *Int. J. Therm. Sci.*, 2010, **49**, 59–66.

19 A. B. D. Cassie and S. Baxter, *Trans. Faraday Soc.*, 1944, **40**, 546.

20 R. N. Wenzel, *Ind. Eng. Chem.*, 1936, **28**, 988–994.

21 D. Murakami, H. Jinnai and A. Takahara, *Langmuir*, 2014, **30**, 2061–2067.

22 E. Bormashenko, *Adv. Colloid Interface Sci.*, 2015, **222**, 92–103.

23 C. Ran, G. Ding, W. Liu, Y. Deng and W. Hou, *Langmuir*, 2008, **24**, 9952–9955.

24 S. Gao, J. Long, W. Liu and Z. Liu, *Langmuir*, 2019, **35**, 9546–9553.

25 C. I. Park, H. E. Jeong, S. H. Lee, H. S. Cho and K. Y. Suh, *J. Colloid Interface Sci.*, 2009, **336**, 298–303.

26 M. Wåhlander, P. M. Hansson-Mille and A. Swerin, *J. Colloid Interface Sci.*, 2015, **448**, 482–491.

27 C. L. Moraila, F. J. Montes Ruiz-Cabello, M. Cabrerizo-Vílchez and M. Á. Rodríguez-Valverde, *J. Colloid Interface Sci.*, 2019, **539**, 448–456.

28 L. Wang, B. Peng and Z. Su, *Langmuir*, 2010, **26**, 12203–12208.

29 S. Min, S. Li, Z. Zhu, W. Li, X. Tang, C. Liang, L. Wang, X. Cheng and W.-D. Li, *Microsyst. Nanoeng.*, 2020, **6**, 106.

30 A. Askounis, K. Sefiane, V. Koutsos and M. E. R. Shanahan, *Colloids Surf. A: Physicochem. Eng. Asp.*, 2014, **441**, 855–866.

31 G. Nagayama and D. Zhang, *Soft Matter*, 2020, **16**, 3514–3521.

32 C. Rohrs, A. Azimi and P. He, *Langmuir*, 2019, **35**, 15421–15430.

33 Y. Kaufman, S.-Y. Chen, H. Mishra, A. M. Schrader, D. W. Lee, S. Das, S. H. Donaldson and J. N. Israelachvili, *J. Phys. Chem. C*, 2017, **121**, 5642–5656.

34 H. Chen, H. Zang, X. Li and Y. Zhao, *Langmuir*, 2019, **35**, 2854–2864.

35 Y. Kita, C. Mackenzie Dover, A. Askounis, Y. Takata and K. Sefiane, *Soft Matter*, 2018, **14**, 9418–9424.

36 X. He, B.-X. Zhang, S.-L. Wang, Y.-F. Wang, Y.-R. Yang, X.-D. Wang and D.-J. Lee, *J. Mol. Liq.*, 2022, **345**, 117049.

37 Z. Wang, D. Orejon, Y. Takata and K. Sefiane, *Phys. Rep.*, 2022, **960**, 1–37.

38 C. Luo, M. Xiang and X. Heng, *Langmuir*, 2012, **28**, 9554–9561.

39 D. I. Yu, S. W. Doh, H. J. Kwak, H. C. Kang, H. S. Ahn, H. S. Park, M. Kiyofumi and M. H. Kim, *Appl. Phys. Lett.*, 2015, **106**, 171602.

40 B. Rofman, S. Dehe, V. Frumkin, S. Hardt and M. Bercovici, *Langmuir*, 2020, **36**, 5517–5523.

41 N. Yu, S. Kiani, M. Xu and C.-J. "CJ" Kim, *Langmuir*, 2021, **37**, 1206–1214.

42 C. Luo and M. Xiang, *Microfluid. Nanofluid*, 2014, **17**, 539–548.

43 D. Zhang and G. Nagayama, *Langmuir*, 2019, **35**, 16508–16513.

44 D. Zhang, S. Takase and G. Nagayama, *J. Colloid . Interface Sci.*, 2021, **591**, 474–482.

45 Thomas Young, *Phil. Trans. R. Soc.*, 1805, **95**, 65–87.

46 F. M. Fowkes, Ed., *Contact Angle, Wettability, and Adhesion*, AMERICAN CHEMICAL SOCIETY, WASHINGTON, D.C., 1964, vol. 43.

47 D. K. Owens and R. C. Wendt, *J. Appl. Polym. Sci.*, 1969, **13**, 1741–1747.

48 D. K. Owens, *J. Appl. Polym. Sci.*, 1970, **14**, 1725–1730.

49 D. H. Kaelble and K. C. Uy, *J. Adhes.*, 1970, **2**, 50–60.

50 A. Kawai, J. Kawakami, and H. Sasazaki, *J. Photopolym. Sci. Technol.*, 2008, **21**, 739–740.

51 K. M. Al Balushi, K. Sefiane and D. Orejon, *J. Colloid Interface Sci.*, 2022, **612**, 792–805.

52 B. Bhushan and Y. Chae Jung, *Ultramicroscopy*, 2007, **107**, 1033–1041.

53 B. He, N. A. Patankar and J. Lee, *Langmuir*, 2003, **19**, 4999–5003.